Fluid Phase Equilibria 430 (2016) 156–168

Contents lists available at ScienceDirect

Fluid Phase Equilibria

journal homepage: www.elsevier.com/locate/fluid

Phase behavior and flow in shale nanopores from molecular simulations

Zhehui Jin [a], Abbas Firoozabadi [a, b, *]

[a] Reservoir Engineering Research Institute, USA
[b] Yale University, USA

ARTICLE INFO

Article history:
Received 4 August 2016
Received in revised form
6 September 2016
Accepted 6 September 2016
Available online 23 September 2016

Keywords:
Shale gas
Nanopores

ABSTRACT

Phase behavior and flow in shale nanopores, due to fluid heterogeneity, cannot be described by bulk and continuum-based formulations. The interactions between fluid and rock molecules are important in both phase behavior and flow. As a result, frameworks from bulk equations of state in phase behavior, and continuum mechanisms and Klinkenberg slippage in flow may become inapplicable. Recently, we have studied both phase behavior and flow in nanopores using density functional theory and various molecular simulations. This work addresses a number of issues related to the adsorption of mixtures of hydrocarbons, carbon dioxide and water as well as methane flow at different pressure conditions in nanopores. For flow, we use the dual control volume-grand canonical molecular dynamics (DCV-GCMD) simulation as in our previous work. We use a smaller pressure difference between high and low pressure reservoirs connected to the nanopores. We find that similar to our past work, the flux of methane in the slit pores can be two orders of magnitude higher than the results from the Hagen-Poiseuille equation.

1. Introduction

Recovery and production from shale reservoirs depend on fluid-in-place and flow in porous media. Fluid phase behavior in shale gas and light oil reservoirs may be drastically different from conventional reservoirs. Unlike conventional rocks, shale is composed of organic (such as kerogen) and inorganic matters (such as clay and quartz). The pores in shale media may be in the nanometer range and both kerogen and clay minerals may contain large amount of fluids in the form of adsorbed molecules [1]. Fluids in shale nanopores may be inhomogeneous and cannot be described as bulk [2]. In addition to adsorption on the rock surface in nanopores, hydrocarbon dissolution in kerogen may also contribute to fluid content in shale permeable media [3]. Fluid flow in shale nanopores is also drastically different from flow in large pores where the Darcy law provides the description. In nanopores, because of fluid inhomogeneity, the Knudsen diffusion and the continuum-based models such as Klinkenberg modification of flow may not apply. In the following, we will discuss our line of attack in phase behavior and flow in shale nanopores.

1.1. Phase behaviors

In a recent work [1], we have divided fluids in shale media into three distinct categories: free molecules, adsorbed molecules, and molecules that move to the kerogen matrix. Free molecules which are present in fractures and large pores behave as bulk fluid. Adsorbed molecules are found near the surfaces of nanometer pores in kerogen and clay minerals. The substrate composition affects the properties of adsorbed molecules. Molecules that move into the kerogen may provide additional fluid-in-place. Kerogen may swell as much as 20% in normal decane and may be more in aromatics [4,5]. For phase behavior description in shale media, we may divide the pores into pores larger than 10 nm, in pores less than 10 nm, and dissolution in kerogen [1].

In pores larger than 10 nm, the contribution from surface adsorption to total fluid in the pores is small. Fluid can be considered homogeneous and critical properties are close to bulk. Mainly the interface curvature affects phase behavior and saturation pressures (bubblepoint or dewpoint). Due to curvature, the dewpoint pressure of rich gas condensates and the amount of liquid dropout often increases. Consequently, less liquid will be produced [1]. On the other hand, the bubblepoint pressure can be suppressed significantly [1,6–9].

In pores less than 10 nm, surface adsorption becomes significant

* Corresponding author. Yale University, USA.
E-mail address: af@rerinst.org (A. Firoozabadi).

http://dx.doi.org/10.1016/j.fluid.2016.09.011
0378-3812/

and confined fluids are heterogeneous. The inhomogeneity arises from confinement and fluid-surface interactions. Phase behavior can be greatly different from the bulk. In small pores, there is no two-phase. At this scale, because the sizes of molecules and nanopores become comparable, fluid-fluid and fluid-surface interactions from molecular perspective should be taken into account. Grand canonical Monte Carlo simulations (GCMC) take into account the inhomogeneity in density distributions and fluid-surface interactions; they are the most common tools to study adsorption and phase behavior of fluids in small nanopores [1,2]. Based on GCMC, we discuss three aspects of phase behavior in small nanopores:

a) Phase Behavior of Confined Hydrocarbon Mixtures from GCMC

Shale gas is generally composed of hydrocarbon mixtures, such as methane, ethane, propane and butane. The phase behaviors of gas mixtures under nano-confinement are very different from bulk. Under confinement, the packaging effect and strong fluid-surface interaction may result in multi-layer adsorption. Recently, a number of experimental and computer simulation studies on phase behavior of confined hydrocarbon mixtures appeared in the literature. Luo et al. [10] measured the confinement effects on the adsorption of binary mixture of octane and decane and observed a clear separation between bubble points of bulk and confined fluids. Pitakbunkate et al. [11] used GCMC simulations to study adsorption of pure and binary mixture of methane and ethane in shale nanopores. They observed shift of critical properties of confined hydrocarbons. Jin and Nasrabadi [12] used Gauge-GCMC simulations to study phase diagram of hydrocarbon binary and ternary mixtures in nanopores and observed that confined effect is stronger for the heavier components than the lighter components. Although computer simulations have been used to study phase diagram of confined hydrocarbon mixtures, the effect of pressure on adsorption of hydrocarbon mixtures has received limited attentions.

In this work, we use GCMC simulations to study adsorption of methane and n-butane binary mixtures in shale nanopores at different pressures. GCMC explicitly takes into account the molecular configurations and orientations which are important for heavier hydrocarbons. The effect of pressure on adsorption in hydrocarbon mixtures can provide important insights into hydrocarbon recovery from shale media.

b) Sorption of CO_2-H_2O mixtures in kerogen nanopores

Shale is composed of two different media: organic and inorganic materials. Organic matter in shale increases effective porosity [13] and can contribute as much as 50% to the total porosity [14]. In addition to organic matter, clay minerals may provide additional sorption capacity due to high internal surface area [15]. A few studies have reported that the clay mineral and its microporous structure may increase gas sorption capacity of organic-rich shales [16–18]. However, organic and inorganic materials have different surface compositions, which can affect adsorption.

Kerogen is generally considered hydrophobic with no charges on the surface, while clay minerals can be hydrophilic with various partially charged atoms on the surface. As a result, water may adsorb differently on the surfaces of these two media. Some shale gas reservoirs are water-saturated [19]. Preloaded water in clay-rich shales significantly reduces gas sorption [20] and even in the organic-rich shales, gas sorption capacity can be greatly reduced because of the moisture [21]. In a previous work, we have shown that even a small amount of water in an outside reservoir can greatly reduce gas sorption in clay nanopores [22]. The methane sorption capacity of other moisture-equilibrated organic materials such as coals is substantially lower than the dry samples [23,24]. In general, water in shale reservoirs is often believed to be associated with clay minerals not kerogen [16]. However, there is no comparison on the effect of water in these two materials on gas adsorption. In this work, we will use the GCMC simulation to study sorption of CO_2-H_2O mixtures in kerogen nanopores and compare with clay minerals.

c) Adsorption selectivity of nC_4 and CO_2

Organic-rich shales may store significant amount of CO_2 via mineral reactions and sorption onto organic matter as well as mineral matter surfaces [25]. Kang et al. [26] predicted that the organic matter in shale can serve for CO_2 sequestration. Injected CO_2 not only could be sequestered in sorbed state but also enhance recovery of natural gas by in-situ molecular swapping mechanism that promotes release and desorption of sorbed gas [26,27]. Yuan et al. [28] used molecular dynamics simulations to study the enhanced recovery of confined methane with CO_2 and found that the injection of CO_2 into the carbon nanotubes can enhance methane recovery at least by 15% over that achieved from pressure drop. Wu et al. [29] also observed that CO_2 can rapidly and efficiently displace adsorbed methane. Kowalczyk et al. [30] observed two-stage process in narrow carbon micropores that the coadsorbed CO_2 can enhance methane adsorption at low CO_2 partial pressure, but reduce methane adsorption due to stronger affinity of CO_2-surface and CO_2-CO_2 interactions as CO_2 partial pressure increases. Although displacement of methane due to the injection of CO_2 has been extensively studied, the effect of CO_2 on heavier hydrocarbon recovery has not been studied yet. The injected CO_2 can lower the viscosity of confined heavier hydrocarbon which can further facilitate the flow. In this work, we use the GCMC simulation to investigate sorption of pure nC_4 and nC_4-CO_2 mixture in kerogen. This study provides insight into heavier hydrocarbon recovery from CO_2 injection.

1.2. Flow in shale media

Shale wells have an early high production rate followed by a rapid decline. Understanding of flow in shale media can help planning and devising various enhancements. Flow in conventional reservoirs can be described by a continuum flow model such as Darcy's law [31–33] and the classical Navier-Stokes equation [34].

At high pressure, the flow may not be described by the Hagen-Poiseuille (HP) equation in nanopores [35]. The HP equation is considered to be valid when the mean free path of molecules is much smaller than the pore size. The HP equation basically describes convective flow and assumes that the velocity of molecules on the surface is zero and ignores surface adsorption. The HP equation for flux J_{HP} in flow direction x in slab geometry of pore size W is given as

$$J_{HP} = -\frac{W^3}{12\mu}\left(\frac{\partial P}{\partial x}\right), \tag{1}$$

where μ is the viscosity and P is pressure. Holt et al. [36] have measured gas and liquid flow in carbon nanotubes of pore sizes of around 2 nm. They show that the measured flux exceeds the prediction from the HP equation by three orders of magnitude. Shale nanopores are similar to carbon nanotubes with the surface being oil-wet; the hydrocarbon molecules tend to adsorb on the surface but not fixed permanently; the adsorbed density distribution is different from the bulk.

When there is slippage at the pore walls, Klinkenberg correction is often applied to the continuum based models. Klinkenberg

correction increases fluid transport. This approach is based on the assumption that there is a thin layer, so-called the Knudsen layer, close to the pore wall in which only collisions between the fluid molecules and wall molecules take place, with fluid-fluid collisions ignored [31]. Klinkenberg assumed that velocity of molecules in the Knudsen layer is non-zero. The slip velocity depends on the permeating fluid, pore pressure and size. The apparent permeability of porous media K_a based on the Klinkenberg effect is given as [37].

$$K_a = K_\infty \left(1 + \frac{b}{P_m}\right), \tag{2}$$

where K_∞ is the absolute permeability at high pressure when the Klinkenberg effect is negligible, b is the fluid slip factor [31,38] and P_m is the mean pore pressure. The Klinkenberg effect is significant when the mean free path of fluid molecules approaches the pore size. Fluid permeability is then enhanced by 'slip flow'. The slip effect can also be incorporated into the HP equation by using a theoretical dimensionless coefficient [39]. The continuum flow with slip effect is given as [35].

$$J^{HP} = -\frac{W^3}{12\eta}\left(\frac{\partial P}{\partial x}\right)\left(1 + \frac{6L_s}{W}\right), \tag{3}$$

where L_s is the slip length, which is the distance extrapolated into the surface to obtain vanishing velocity as assumed by no-slip boundary condition [35,40]. When the calculated slip length is much larger than the pore width, the continuum-based equations would not give accurate results [36]. The calculated slip length in sub-2 nm pore can be three orders of magnitude larger than the pore size [36], which indicates that slip-flow formalism may not be applicable to flow in nanopores.

Molecular simulation is the best option to take into account the inhomogeneous fluid density in nanopores. A number of groups [41–44] report that low density diffusion coefficient in silica nanopores is as much as one order of magnitude smaller than that from the Knudsen diffusion equation. Zeolites and silicates have three-dimensional amorphous structures. Flow in these media may not fulfill the assumption of long nanopores in the Knudsen approach. At reservoir condition, pressure can be over a few hundred bar making the Knudsen diffusion inapplicable [35]. Recently, there are a number of molecular simulations works on hydrocarbon flows in shale nanopores [45–48] indicating that molecular velocity on the pore surface is non-zero, which enhances flow. In a recent work, by using the dual control volume-grand canonical molecular dynamics simulation (DCV-GCMD), we found that methane flux in carbon nanopores of length up to 150 nm can be one to two orders of magnitude higher than that from HP equation for high pressure methane flow between bulk reservoir pressures at 100 and 70 bar at room temperature [35]. We used a high pressure drop between the inlet and outlet of the carbon nanotube.

In this work, we use the DCV-GCMD simulations to study high pressure flow with smaller pressure difference in high and low pressure conditions. The objective is to find out whether one to two orders of magnitude increase over the HP equation is due to high pressure drop.

The remainder of this paper is organized as follows. In Molecular Model and Theory, we present the molecular simulation and theory methods and define molecular models used in this work. In Results and Discussion, we cover: (1) phase behavior in pores less than 10 nm and (2) methane flow in shale nanopores. In pores less than 10 nm, we will investigate the phase behavior predictions from GCMC in mixtures of C_1-nC_4, CO_2-H_2O, and nC_4-CO_2. In Conclusions, we summarize the key findings and discuss implications.

2. Simulation method

2.1. Grand canonical Monte Carlo simulation

One effective method to study phase behavior of hydrocarbon fluids in nanopores is to use the GCMC simulations. In an open system, there would be exchange of energy and matter with surroundings. We assume that nanopores are connected to a reservoir where the chemical potentials μ, system volume V and temperature T are fixed. The chemical potential represents bulk fluid condition. For a given bulk fluid at given pressure and temperature, the chemical potentials of each component are obtained from Widom's particle insertion method [49] from NVT simulation. We use chemical potentials of each component to represent the bulk fluid at given pressure and temperature which is in equilibrium with confined media. Because the number of molecules within the volume fluctuates throughout the simulation, the ensemble averaged number of molecules is fully determined by the chemical potentials.

For hydrocarbon molecules, we use the TraPPE force field to describe the non-bonded interactions U between pseudo-atoms, which are separated by more than three bonds or belong to different molecules, solely based on pairwise-additive Lennard-Jones (LJ) 12-6 potentials [50],

$$U(r_{ij}) = 4\varepsilon_{ij}\left[\left(\frac{\sigma_{ij}}{r_{ij}}\right)^{12} - \left(\frac{\sigma_{ij}}{r_{ij}}\right)^{6}\right], \tag{4}$$

where r_{ij}, ε_{ij}, and σ_{ij} are the separation, LJ well depth, and LJ size, respectively, for the pair of atoms i and j. The parameters ε and σ are 98 K and 0.375 nm, respectively, for the methyl group (-CH_3), 46 K and 0.395 nm, respectively, for the methylene group (−CH_2−), and 148 K, 0.373 nm, respectively, for CH_4. Unlike interactions are computed using the standard Lorentz-Berthelot combining rules. The bond length is 0.154 nm. Bond-bending potentials U_{bend} are given as [51].

$$U_{bend}(\theta) = \frac{K_\theta}{2}(\theta - \theta_{eq})^2, \tag{5}$$

where $K_\theta = 62500$ K/rad^2 and $\theta_{eq} = 114°$. Torsion energy U_{tor} is based on the OPLS united atom torsional potential [52].

$$U_{tor}(\varphi) = V_0 + V_1(1 + \cos\varphi) + V_2(1 - \cos 2\varphi) + V_3(1 + \cos 3\varphi), \tag{6}$$

where φ is the torsion angle, $V_0 = 0$, $V_1 = 355.03$ K, $V_2 = -68.19$ K, and $V_3 = 791.32$ K.

Water molecules are simulated using the SPC [53] model. The pairwise additive Lennard-Jones and Coulomb potentials are used to compute the intermolecular interactions

$$u(r_{ij}) = u^{LJ} + u^{C} = 4\varepsilon_{ij}\left[\left(\frac{\sigma_{ij}}{r_{ij}}\right)^{12} - \left(\frac{\sigma_{ij}}{r_{ij}}\right)^{6}\right] + \frac{q_i q_j}{4\pi\varepsilon_0 r_{ij}}, \tag{7}$$

in which q_i is the partial charge of the site and $\varepsilon_0 = 8.854 \times 10^{-12}$ F/m is the electric constant. The conventional Lorentz-Berthelot combining rules are applied to the LJ parameters.

For CO_2 molecules, we use the flexible three-site EPM2 model [54], which includes the bond-bending potential, the short-range LJ potential, and the long-range Coulomb potential. The bond-bending potential U_{bend} of CO_2 molecule is given by Eq. (5) with constants [54] $K_\theta = 1236$ KJ/mol/rad^2, θ is the bond-bending angle

between O–C–O atoms, and $\theta_{eq} = \pi$ rad is the equilibrium bond-bending angle. The parameters of CO_2 and water molecules are given in Table 1. All of the short-range LJ interactions are truncated at a distance of 1.07 nm and the long-range electrostatic interactions are treated by means of *Ewald* summation with the correction term [55,56] for the periodic boundary condition in *x*,*y* planes.

In this work, pores are of slit geometry with smooth and structureless surfaces. We use 10-4-3 Steele potentials to describe the fluid-wall interaction φ_{wf} [57].

$$\varphi_{wf}(z) = 2\pi\rho_w\varepsilon_{wf}\sigma_{wf}^2\Delta\left[\frac{2}{5}\left(\frac{\sigma_{wf}}{z}\right)^{10} - \left(\frac{\sigma_{wf}}{z}\right)^4 - \frac{\sigma_{wf}^4}{3\Delta(0.61\Delta + z)^3}\right], \tag{8}$$

where $\rho_w = 114$ nm^{-3}, $\varepsilon_w = 28$ K, $\sigma_w = 0.3345$ nm, and $\Delta = 0.335$ nm, respectively. The external potential Ψ in a slit pore is expressed as

$$\Psi(z) = \varphi_{wf}(z) + \varphi_{wf}(H - z), \tag{9}$$

where H is the slit-pore size.

2.2. Dual control volume-grand canonical molecular dynamics simulation

In our simulations, the slit nanopore is placed between two bulk reservoirs at two different pressures at constant temperature. Kerogen is hydrophobic and may be simulated by carbon materials [2]. We use full atomistic structure of graphite layers formed by carbon atoms to simulate nanopores as in our previous work [35]. Both methane molecules and carbon atoms are modeled by the single-site Lennard-Jones (LJ) particles to describe the dispersion interactions.

The box used in simulations consists of five regions as shown in Fig. 1. The **H**, **L** and **C** regions correspond to the high and low chemical potential control volumes (CV), and carbon nanopores, respectively. We apply periodic boundary condition in all three directions. The **H** regions are placed at the two ends and **L** region is placed in the middle of the box. The **C** regions are placed between the two control volumes. The sizes of **H** and **L** regions in the *x* direction are fixed at 20 nm. The carbon atoms are placed according to the structure of graphite layers [58,59] to construct the nanopores. We use three graphite layers to form one carbon sheet and two carbon sheets to set up the slit-like pores. The separation distance between carbon atom centers of two graphite layers is $\Delta = 0.335$ nm. The distance between two adjacent carbon atoms in the same graphite layer is $L_{cc} = 0.142$ nm. The schematics of graphite layer and carbon sheet are shown in Fig. 2. Carbon sheet positions are fixed throughout the simulation. The box size is $(40 + 2 \times L_c)$nm $\times$ 4.92 nm $\times$ $(1.675 + W)$nm in the *x*, *y* and *z* directions, respectively, where L_c is the length of nanopores and W is the pore width, which is the separation distance between the centers of carbon atoms of the two layers forming a slit pore. The length of nanopores in the *y* direction is the same as the box size (4.92 nm). The origin is set at the center of the simulation box.

Table 1
Parameters of CO_2 and water molecules for GCMC.

Atom	ε (K)	σ (nm)	q (e)
Carbon dioxide			
C	28.129	0.2757	0.6512
O	80.507	0.3033	−0.3256
Water			
H	0	0	0.41
O	78.18	0.3166	−0.82

We use the TraPPE model [50] to simulate methane molecules. Unlike interactions are computed using the standard Lorentz-Berthelot combining rules. The size parameter σ and energy parameter ε are 0.373 nm and 148 K for methane and 0.34 nm and 28 K for carbon atoms. All of the LJ interactions are truncated at a distance of 1.07 nm. Due to the truncation, molecules in slit pores do not interact with their images. The interaction between a methane molecule and carbon atoms is obtained by summing over all carbon atoms in the nanopores.

Throughout the simulation volume, standard molecular dynamics (MD) simulation moves are employed. The equations of motion are solved by the Verlet velocity algorithm [60] using the Berendsen thermostat [61] to maintain constant temperature. Linked cells [62] are employed to reduce the computation time. The chemical potential of methane in the CVs is maintained using a sufficient number of GCMC insertions and removals [63–65]. The probability of inserting a methane molecule p^+ is given by

$$p^+ = \min\left\{\frac{ZV_{CV}}{N_{CV}+1}\exp\left(-\frac{\Delta U}{k_BT}\right), 1\right\}, \tag{10}$$

where $Z = \exp(\mu/k_BT)/\Lambda^3$ is the absolute activity at temperature T, Λ is the de Broglie wavelength, μ is the chemical potential, k_B is the Boltzmann's constant, ΔU is the potential energy change resulting from inserting or removing a molecule, V_{CV} is the volume of CV and N_{CV} is the number of methane molecules in each CV. As the particles are inserted, the Maxwell-Boltzmann distribution [66] is used to assign velocities. The probability of removing a molecule p^- is given by

$$p^- = \min\left\{\frac{N_{CV}}{ZV_{CV}}\exp\left(-\frac{\Delta U}{k_BT}\right), 1\right\}. \tag{11}$$

100 GCMC moves in each CV are followed by one MD integration step [31]. After particle insertion/removal, we use Verlet velocity algorithms to calculate forces acting on the molecules. The chemical potentials are obtained from Widom's particle insertion method [49] in the independent *NVT* Monte Carlo simulations of bulk methane fluid. The time step of MD simulation is $\Delta t = 2$ fs. We use 10 ns simulation time for system to reach steady state and 20 ns simulation time to calculate density, velocity profiles and fluxes. The system temperature is fixed at 298.15 K.

The flux of methane molecules J_x in the *x* direction is computed by counting the net number of particles crossing halfway along each nanopore region [63,67]:

$$J_x = \frac{n^{hl} - n^{lh}}{n_t\Delta t A_{yz}}. \tag{12}$$

where n^{hl} and n^{lh} are the number of molecules moving from high to low pressure region and vice versa, n_t is the number of time step of sampling, A_{yz} is the cross-section area of carbon nanopore. The final estimate of the flux is the average of the flux in the two nanopore regions.

3. Results and discussions

In our simulations, the pressure represents the bulk pressure of the fluid in equilibrium with confined media.

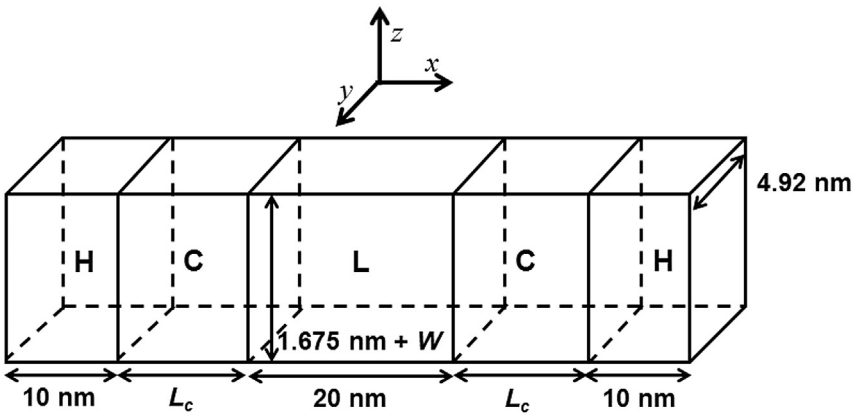

Fig. 1. Schematic representation of simulation box. The molecules flow along the *x*-direction.

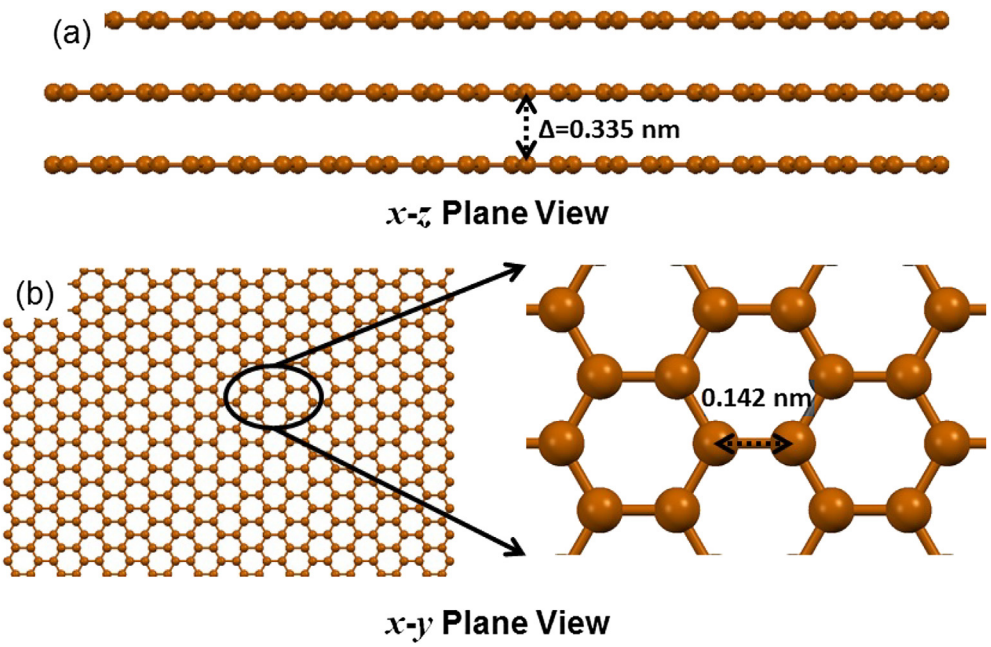

Fig. 2. Schematic representation of carbon sheet; (a) *x-z* plane view; (b) *x-y* plane view. Carbon atom size does not scale to LJ parameters.

3.1. Phase behaviors

a) Hydrocarbon mixtures adsorption from GCMC

In this section, we study the adsorption of C_1-nC_4 mixtures in nanopores. C_1 molecules are represented as spherical particles. However, orientation and configuration of nC_4 may affect fluid sorption and phase behavior in nanopores. We use an atomistic representation for nC_4.

In Fig. 3, we present density profiles of a mixture of C_1-nC_4 (0.9/0.1, mole) at $T = 368.15$ K in 1 nm pores at different pressures. Note that the composition and pressure are fixed in the outside reservoir. Both C_1 and nC_4 form adsorption layers on the surface. Because surface attraction of nC_4 is stronger than methane, adsorption of nC_4 is greatly enhanced. As pressure drops, C_1 sorption decreases, but nC_4 sorption increases. At lower pressure, the competition from C_1 molecules becomes weaker, so nC_4 is more readily adsorbed in the pores. Similar trend has been reported in the study of adsorption of hydrocarbon mixtures in zeolites [68] and pillared layered materials [69].

In Fig. 4, we present density profiles of the C_1-nC_4 mixture (0.9/0.1, mole) at $T = 368.15$ K in 3 nm pores. Similar to 1-nm pores, both C_1 and nC_4 form adsorption layers on the surface and weak second adsorption layers. As pressure drops, nC_4 density increases but C_1 density decreases. Such behavior indicates that in the production, as pressure drops, it is the lighter components that are more easily produced, while the heavier components may tend to stay within the nanopores. This phenomena also suggest that gas injection such as CO_2, may help to produce heavier component from nanopores, which we will discuss later.

b) Adsorption of pure nC_4 and nC_4-CO_2 mixtures

We use GCMC to investigate sorption of pure nC_4 and an equimolar mixture of nC_4-CO_2. By comparing sorption of pure nC_4 and equimolar mixture of nC_4-CO_2 mixture, we develop an understanding toward recovery of heavier hydrocarbons by CO_2 injection.

We present the density distributions of pure nC_4 and an equimolar mixture of nC_4-CO_2 in 1-nm pores at $T = 368.15$ K as shown in Fig. 5. Small pores are readily saturated by pure nC_4 due to strong

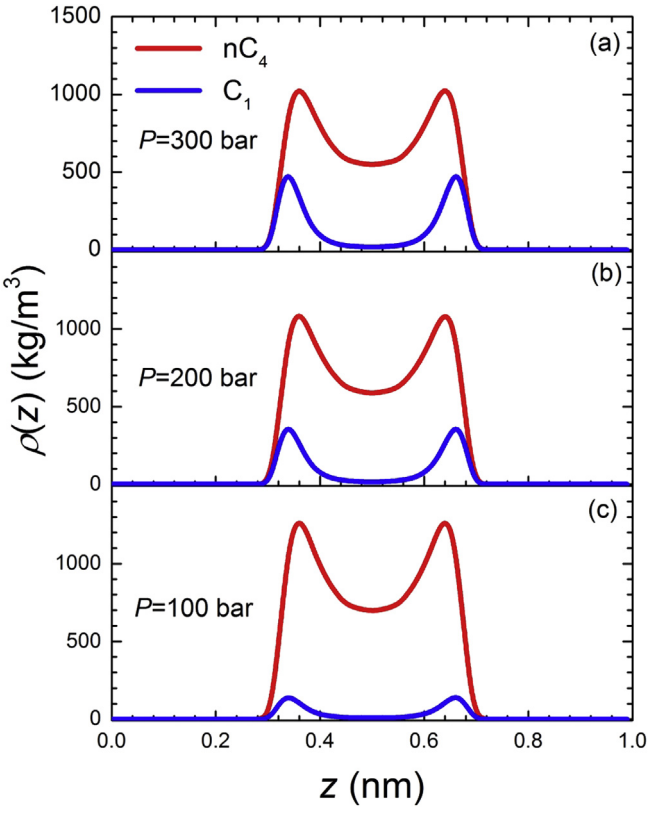

Fig. 3. Density profiles of C_1-nC_4 mixture (0.9/0.1, mole) at (a) $P = 300$ bar, (b) $P = 200$ bar, and (c) $P = 100$ bar in 1 nm pores at $T = 368.15$ K.

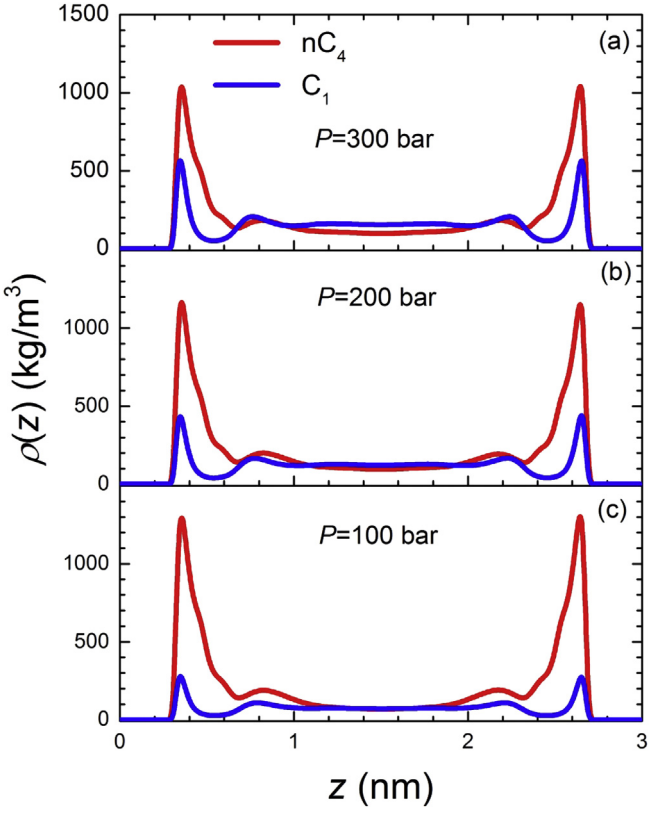

Fig. 4. The same as Fig. 3, but in 3 nm pores.

surface attractions; as pressure increases, nC_4 sorption increases negligibly. For the nC_4-CO_2 mixture, as pressure increases, nC_4 sorption decreases, but CO_2 sorption increases. At low pressures, because nC_4 molecules have stronger affinity to surface than CO_2 molecules, nC_4 sorption is stronger than CO_2. At high pressures, association of CO_2 becomes stronger. As a result, CO_2 molecules are adsorbed on the surface. nC_4 molecules form adsorption layer beyond the adsorption layer of CO_2 molecules, because CO_2 molecule is smaller than nC_4 molecule. The effect of CO_2 on the recovery of nC_4 from nanopores is more significant at higher pressures.

Slightly different behavior is observed in larger pores as shown in the density distributions of pure nC_4 and the equimolar nC_4-CO_2 mixture in 3-nm pores in Fig. 6. For pure nC_4, sorption increases with pressure; for nC_4-CO_2 mixture, while CO_2 sorption increases with pressure, nC_4 sorption increases with pressure then decreases. At low pressure ($P = 10$ bar), nC_4 has strong adsorption layer and weak second adsorption layer, but density in the middle of pores is close to vapor phase for the nC_4-CO_2 mixture; pure nC_4 has multi-layer adsorption in the pores. As a result, reduction in nC_4 sorption is significant. As pressure increases, nC_4 has multi-layer adsorption in the nC_4-CO_2 mixture. However, as CO_2 sorption increases, nC_4 sorption decreases. At high pressures, CO_2 also has multi-layer adsorption and reduction of nC_4 is significant.

c) Adsorption of CO_2-H_2O mixtures

Some shale gas reservoirs may be water-saturated [19]. Pre-loaded water in clay-rich shales significantly reduces gas sorption [3]. Kerogen is generally hydrophobic, but clay minerals are hydrophilic; water or moisture in shale is mainly associated with clay minerals [16]. Experimental and computational investigations [16,22] have shown that water can significantly reduce gas sorption in clay minerals. A small amount of water in the outside reservoir can greatly reduce CO_2 sorption in clay nanopores [22]. Due to partial charges on the clay surfaces, water molecules are predominantly adsorbed on the surfaces hindering the formation of gas adsorption layer [22].

In this work, we use carbon nanopores to represent kerogen nanopores to study adsorption in mixtures of CO_2—H_2O by GCMC. In contrast to clay, there is no charge effect in carbon nanopores. There may be heteroatoms and functional groups on the surface of kerogen. But we assume that kerogen has similar properties as carbon materials.

In Fig. 7, we show the density distributions of CO_2 and H_2O molecules in carbon nanopores at bulk pressure $P = 125$ bar in different pore sizes at $T = 348.15$ K. The computations are based on the chemical potentials in a CO_2-rich phase with CO_2 mole fraction $x_{CO_2} = 0.994$. In all cases, CO_2 molecules are sorbed in the pores but H_2O sorption is negligible. Without surface charges, carbon behaves as a hydrophobic material. As a result, H_2O sorption in carbon nanopores is greatly reduced; CO_2 sorption is not affected by H_2O in the outside reservoir. In small pores ($H = 1$ nm), because two walls are close, CO_2 forms one adsorption layer near the surfaces. In larger pores ($H \geq 2$ nm), it has multi-adsorption layer structures: a strong first adsorption layer, second layer and filling in the middle of the pores.

In Fig. 8, we show the density distributions of CO_2 and H_2O molecules of H_2O-rich phase with CO_2 mole fraction $x_{CO2} = 0.012$ in the outside reservoir at bulk pressure $P = 125$ bar in different pore sizes at $T = 348.15$ K. In small pores ($H = 1$ nm), only CO_2 adsorbs in the pores, because carbon surfaces are hydrophobic. In larger pores ($H \geq 2$ nm), H_2O forms liquid-like phase in the middle and CO_2 forms an adsorption layer near the surface. As the pore size increases, H_2O adsorption increases, because the effect of hydrophobic surface becomes less significant. The adsorption layer of CO_2

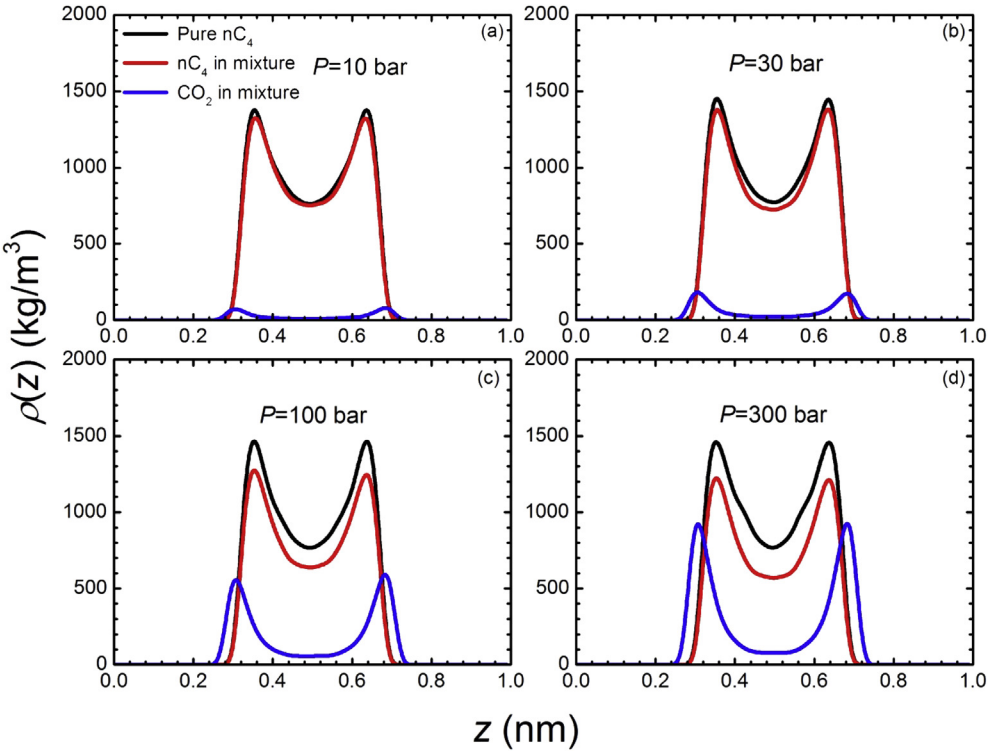

Fig. 5. Density profiles of pure nC_4 and equimolar CO_2-nC_4 mixture at (a) $P = 10$ bar, (b) $P = 30$ bar, (c) $P = 100$ bar, and (d) $P = 300$ bar in 1 nm pores at $T = 368.15$ K from GCMC.

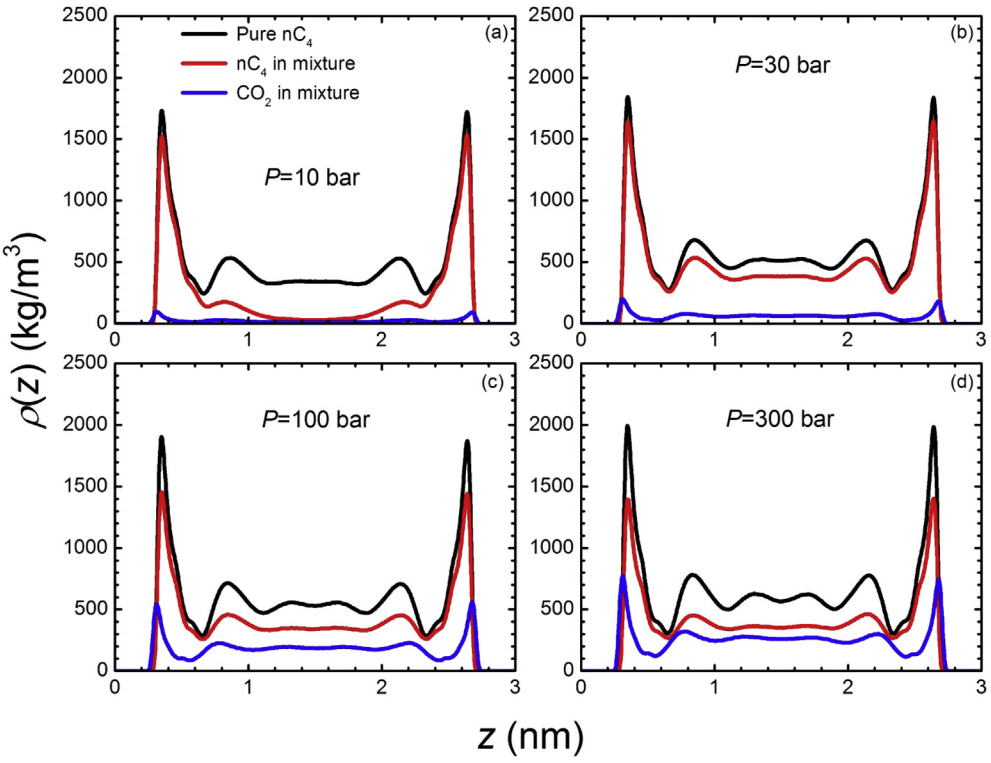

Fig. 6. The same as Fig. 5, but in 3 nm pores.

increases the solubility of CO_2 in water in nanopores. The comparison between CO_2-H_2O mixture sorption in clay and carbon nanopores clearly indicates that H_2O molecules are less likely adsorbed in hydrophobic kerogen nanopores but predominately in clay nanopores.

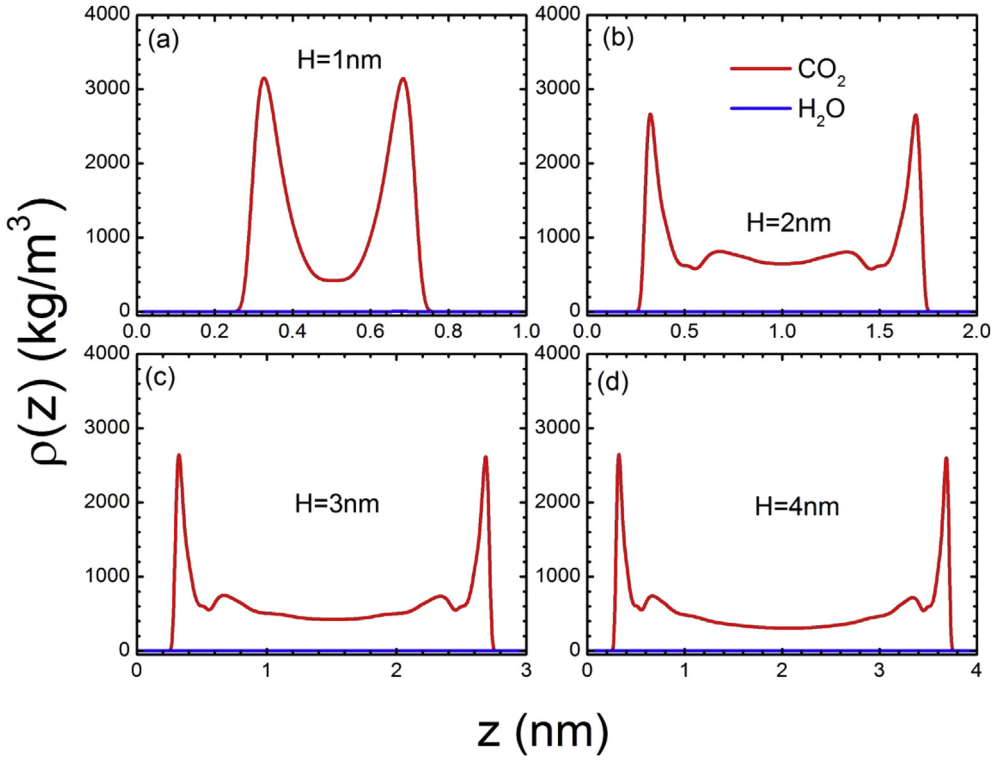

Fig. 7. The density distributions of CO_2 and water molecules for reservoir of CO_2 mole fraction $x_{CO_2} = 0.994$ at bulk pressure $P = 125$ bar and temperature $T = 348.15$ K in carbon nanopores of (a) $H = 1$ nm. (b) $H = 2$ nm. (c) $H = 3$ nm. (d) $H = 4$ nm. The red and blue lines represent the CO_2 density distribution and the water density distribution, respectively. (For interpretation of the references to colour in this figure legend, the reader is referred to the web version of this article.)

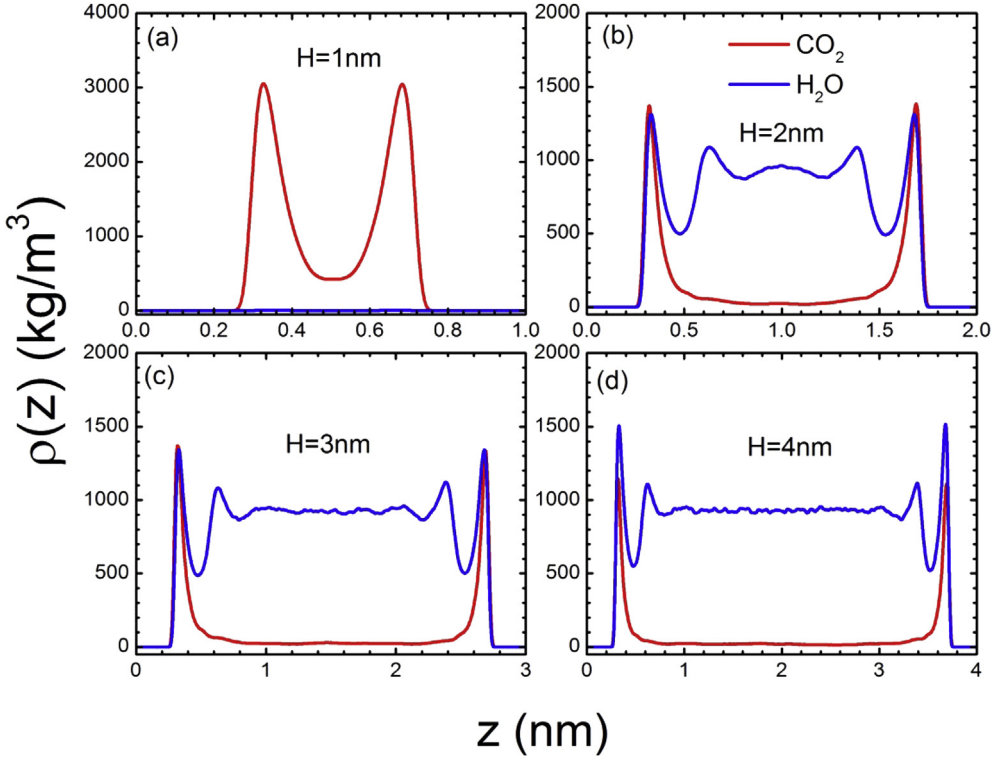

Fig. 8. The same as Fig. 7, but for CO_2 mole fraction $x_{CO_2} = 0.012$.

3.2. Flow in shale media

In this section, we present methane flow in carbon nanopores between two bulk reservoirs by using DCV-GCMD. In Fig. 9, we present the methane molecular flux from higher pressure of $P_h = 80$ bar to low pressure of $P_l = 70$ bar and higher pressure of $P_h = 200$ bar to low pressure of $P_l = 190$ bar in the control volumes in different pore widths and lengths. For comparison, we also show the predictions from the HP equation. We assume linear pressure drop in the HP equation from Eq. (1),

$$J_{HP} = -\frac{W^3}{12\mu}\frac{P_l - P_h}{L_c}. \tag{13}$$

The flux from the DCV-GCMD simulations is higher than that from HP equation for pore sizes less than 4 nm. For $W = 1$ nm, the enhancement can be more than two orders of magnitude. For $W = 4$ and 10 nm, the flux from DCV-GCMD of $P_h = 200$ bar is higher than that of $P_h = 80$ bar with the same pressure difference, but the opposite is true for $W = 1$ and 2 nm. The flux in nanopore is dependent on the molecular density profile and velocity [35]. Methane has stronger adsorption layer in small nanopore, but lower molecular velocity; in large nanopores, the higher molecular velocity, but weaker adsorption layer. On the other hand, HP equation predicts that methane flow in nanopores increases with pressure. Two orders of magnitude higher flux than HP equation is attributed to flow of the adsorbed layer and inhomogeneous distributions of methane molecules inside the nanopores. In the following, we investigate density and velocity profiles in different pore widths and pressures.

3.2.1. Density profiles

In Fig. 10, we present density profiles of methane molecules at different positions of pores of $L_c = 136.178$ nm for flow between $P_h = 80$ bar and $P_l = 70$ bar. For comparison, we also show the average bulk density ρ_a^b based on the inlet and outlet reservoirs,

$$\rho_a^b = \frac{1}{2}\left(\rho_h^b + \rho_l^b\right), \tag{14}$$

where ρ_h^b and ρ_l^b are bulk density at the inlet and outlet reservoirs, respectively. Methane molecules are adsorbed on the surfaces forming a strong adsorption layer and weak second adsorption layer throughout the pores. The density distributions at different positions of pores are similar. For $W \leq 2$ nm, methane density in nanopores is higher than ρ_a^b; for $W \geq 4$ nm, methane density in the middle of pores is close to ρ_a^b. We also present density profiles of methane molecules at different positions of pores of $L_c = 136.178$ nm for flow between $P_h = 200$ bar and $P_l = 190$ bar in Fig. 11. Methane forms strong first and second adsorption layers and a weak third adsorption layer in nanopores. The methane density in nanopores of $P_h = 200$ bar and $P_l = 190$ bar is higher than that of $P_h = 80$ bar and $P_l = 70$ bar. Similar to Fig. 10, the density in the middle of the pores are close to ρ_a^b.

3.2.2. Velocity profiles

In Fig. 12, we graph the velocity distributions of methane in the x direction at different positions of pores of $L_c = 136.178$ nm for flow between $P_h = 80$ bar and $P_l = 70$ bar. For clarity, we also point out the location of the strongest adsorption layers. The velocity on the surface is non-zero and comparable to that in the middle of the pores; adsorption layer is moving along the flow direction. On the other hand, the continuum flow model assumes that velocity on the surface is zero and density distribution is homogeneous in nanopores. Coupling with inhomogeneous density distribution, strong adsorption layers and non-zero velocity on the surface, the flow from DCV-GCMD can be two orders of magnitude larger than that from HP equation. Molecular velocity increases with pore size. In

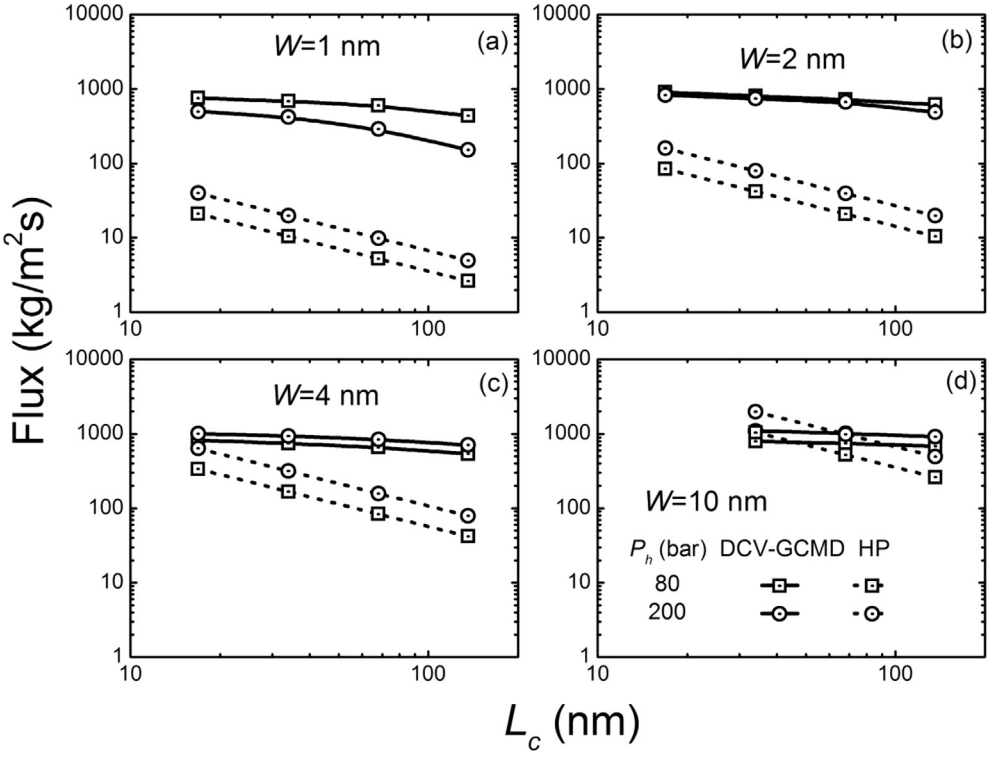

Fig. 9. Methane molecular fluxes from DCV-GCMD and HP equation.

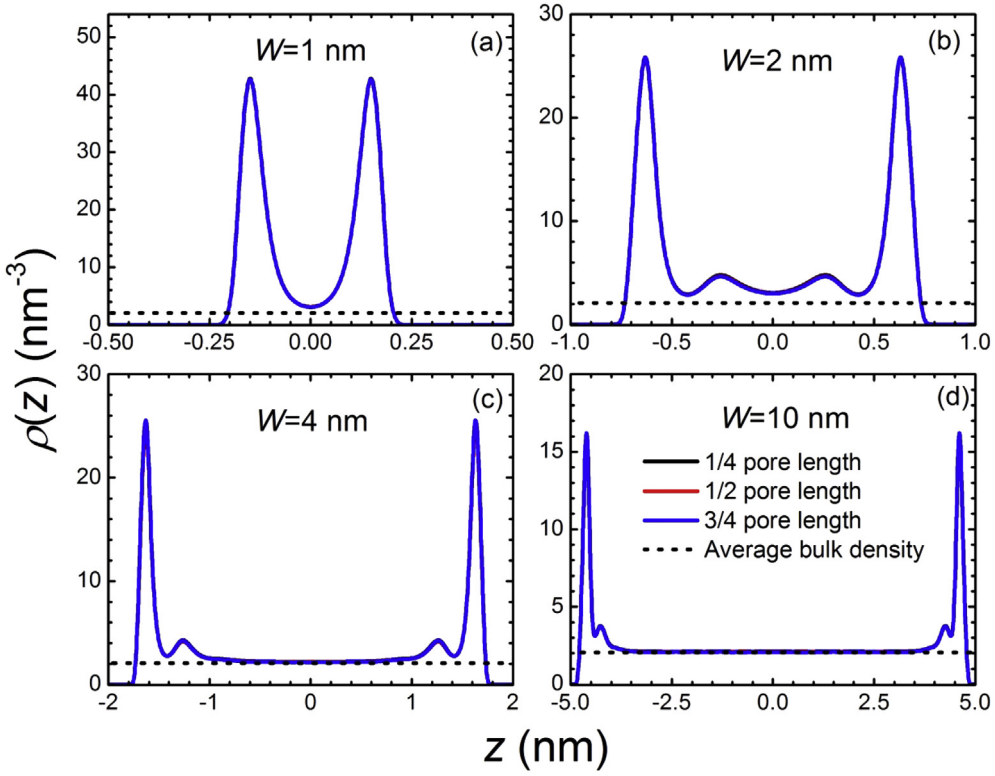

Fig. 10. (a) Density profiles at the 1/4, 1/2, 3/4 lengths in nanopores between control volume pressure $P_h = 80$ bar and $P_l = 70$ bar of $L_c = 136.178$ nm and $W = 1$ nm; (b) $W = 2$ nm; (c) $W = 4$ nm; (d) $W = 10$ nm pores. For comparison, we also show the average bulk density.

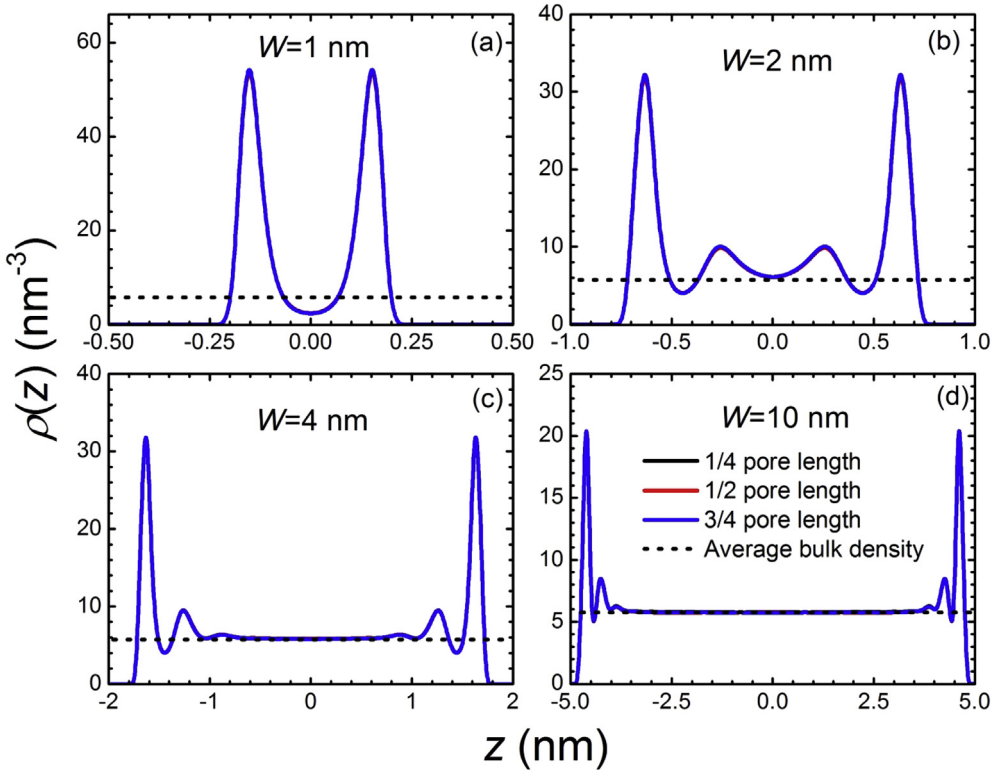

Fig. 11. (a) Density profiles at the 1/4, 1/2, 3/4 lengths in nanopores between control volume pressure $P_h = 200$ bar and $P_l = 190$ bar of $L_c = 136.178$ nm and $W = 1$ nm; (b) $W = 2$ nm; (c) $W = 4$ nm; (d) $W = 10$ nm pores. For comparison, we also show the average bulk density.

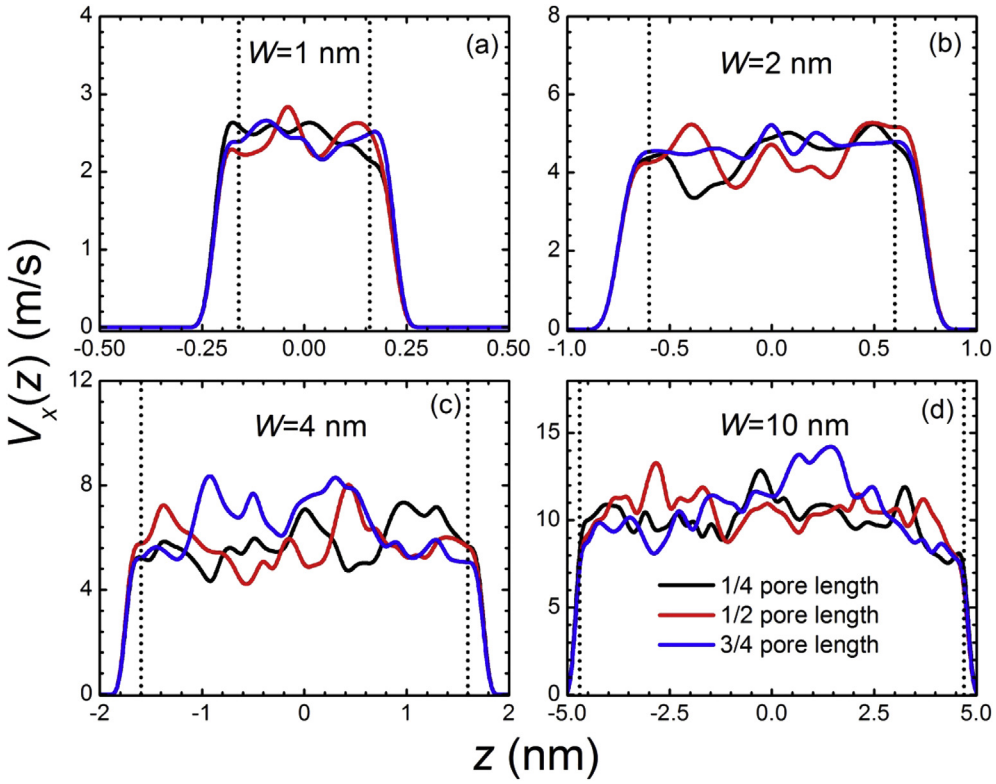

Fig. 12. (a) Velocity profiles in x direction at the 1/4, 1/2, 3/4 lengths in nanopores between control volume pressure $P_h = 80$ bar and $P_l = 70$ bar of $L_c = 136.178$ nm and $W = 1$ nm; (b) $W = 2$ nm; (c) $W = 4$ nm; (d) $W = 10$ nm pores. We also show the locations of the strongest adsorption layer by dotted lines.

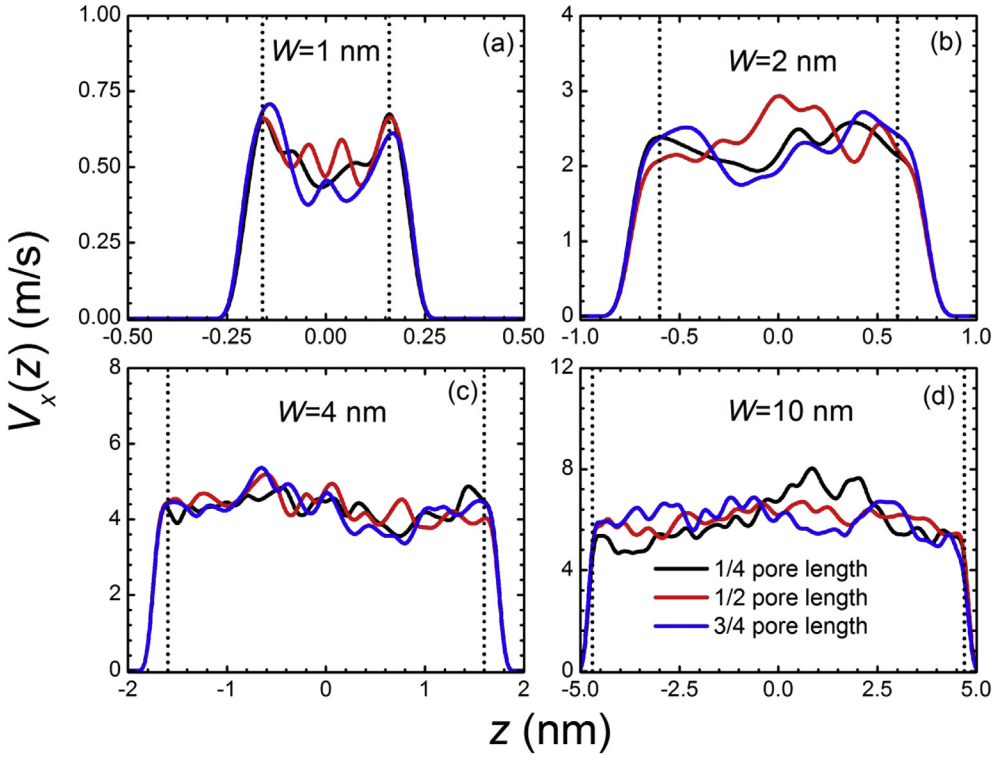

Fig. 13. (a) Velocity profiles in the x direction at the 1/4, 1/2, 3/4 lengths in nanopores between control volume pressure $P_h = 200$ bar and $P_l = 190$ bar of $L_c = 136.178$ nm and $W = 1$ nm; (b) $W = 2$ nm; (c) $W = 4$ nm; (d) $W = 10$ nm pores. We show he locations of the strongest adsorption layer by dotted lines.

small nanopores, molecules are more compact than in large pores. We present velocity distributions of methane in the x direction at different positions of pores of $L_c = 136.178$ nm for flow between $P_h = 200$ bar and $P_l = 190$ bar in Fig. 13. In contrast to flow between $P_h = 80$ bar and $P_l = 70$ bar, molecular velocity is lower in nanopores due to higher densities. Again, the molecular velocity on the surface is non-zero and the mobility of adsorption layer greatly enhances flow in nanopores. For $W = 1$ nm, velocity on the surface is slightly higher than that in the middle of the pores. As shown in Fig. 11, methane molecules mainly adsorb on the surface and there are much fewer molecules in the middle of the pores. Thus, in such small nanopores, methane molecules mainly flow through adsorption layer. When $W \geq 2$ nm, molecular velocity on the surface is comparable to that in the middle of the pores.

4. Conclusions

In this work, we used GCMC simulations to study adsorption of mixtures and DCV-GCMD simulations to investigate methane flow in shale nanopores.

The adsorption of C_1-nC_4 indicates that in small nanopores, as pressure decreases, lighter component adsorption decreases, but heavier component adsorption increases. This behavior shows that as pressure drops, the heavier component may not be readily produced from nanopores. We also studied CO_2–H_2O mixture adsorption in carbon nanopores and found that due to hydrophobic surfaces, CO_2 dominates in nanopores. The comparison to clay nanopores indicates that H_2O molecules are less likely adsorbed in hydrophobic kerogen nanopores but predominately in clay nanopores. The adsorption of pure nC_4 and nC_4-CO_2 mixture indicates that when pore size is small ($H = 1$ nm), CO_2 injection may help recovery of heavier hydrocarbons only at high pressure condition. However, when pore size is larger ($H = 3$ nm), CO_2 injection can help recovery of heavier hydrocarbons from nanopores at low ($P = 10$ bar) or high pressure ($P = 300$ bar) conditions due to different reasons. At low pressure, the injection of CO_2 can prevent the capillary condensation of nC_4; at high pressure, the competition from CO_2 adsorption reduces nC_4 adsorption.

Methane flow in carbon slit pores is considerably enhanced in small pore size and long length. The increase in flow can be more than two orders of magnitudes compared to HP equation. Our results at low pressure difference between the two ends of the slit pore are in agreement with high pressure difference results. For $W = 1$ nm, molecular flux decreases with pressure; for $W \geq 4$ nm, flux increases with pressure. Overall, when $W \geq 2$ nm, fluxes between $P_h = 80$ bar and $P_l = 70$ bar and between $P_h = 200$ bar and $P_l = 190$ bar are comparable.

The findings from molecular simulations of phase behavior and flow can be converted into simple expressions for use in the conventional reservoir simulations after we study various fluids and rocks extensively.

Acknowledgement

This work was supported by member companies of the Reservoir Engineering Research Institute. Their support is greatly appreciated.

References

[1] Z. Jin, A. Firoozabadi, Thermodynamic modeling of phase behavior in shale media, SPE J. 21 (1) (2016) 190–207.
[2] Z. Li, Z. Jin, A. Firoozabadi, Phase behavior and adsorption of pure substances and mixtures and characterization in nanopore structures by density functional theory, SPE J. 19 (6) (2014) 1096–1109.
[3] D.J.K. Ross, R. Bustin, The importance of shale composition and pore structure upon gas storage potential of shale gas reservoirs, Mar. Petroleum Geol. 26 (6) (2009) 916–927.
[4] J.W. Larsen, S. Li, Solvent swelling studies of green river kerogen, Energy & Fuels 8 (4) (1994) 932–936.
[5] D. Ertas, S.R. Kelemen, T.C. Halsey, Petroleum expulsion Part 1. Theory of kerogen swelling in multicomponent solvents, Energy & Fuels 20 (1) (2006) 295–300.
[6] L. Chu, et al., Characterizing and simulating the nonstationariness and nonlinearity in unconventional oil reservoirs: bakken application, in: SPE Canadian Unconventional Resources Conference, Society of Petroleum Engineers, Calgary, Alberta, Canada, 2012.
[7] L. Du, L. Chu, Understanding anomalous phase behavior in unconventional oil reservoirs, in: SPE Canadian Unconventional Resources Conference, Society of Petroleum Engineers Calgary, Alberta, 2012.
[8] Y. Wang, B. Yan, J. Killough, Compositional modeling of tight oil using dynamic nanopore properties, in: SPE Annual Technical Conference and Exhibition, Society of Petroleum Engineers, New Orleans, LA, 2013.
[9] B. Nojabaei, R.T. Johns, L. Chu, Effect of capillary pressure on phase behavior in tight rocks and shales, SPE Reserv. Eval. Eng. 16 (3) (2013) 281–289.
[10] S. Luo, H. Nasrabadi, J.L. Lutkenhaus, Effect of confinement on the bubble points of hydrocarbons in nanoporous media, AIChE J. 62 (5) (2016) 1772–1780.
[11] T. Pitakbunkate, et al., Effect of confinement on pressure/volume/temperature properties of hydrocarbons in shale reservoirs, SPE J. 21 (02) (2016) 621–634.
[12] B. Jin, H. Nasrabadi, Phase behavior of multi-component hydrocarbon systems in nano-pores using gauge-GCMC molecular simulation, Fluid Phase Equilibria 425 (2016) 324–334.
[13] T. Zhang, et al., Effect of organic-matter type and thermal maturity on methane adsorption in shale-gas systems, Org. Geochem. 47 (0) (2012) 120–131.
[14] C.H. Sondergeld, et al., Micro-structural Studies of Gas Shales, Society of Petroleum Engineers, 2010, p. 131771.
[15] M. Gasparik, et al., Geological controls on the methane storage capacity in organic-rich shales, Int. J. Coal Geol 123 (2014) 34–51.
[16] L. Ji, et al., Experimental investigation of main controls to methane adsorption in clay-rich rocks, Appl. Geochem. 27 (12) (2012) 2533–2545.
[17] R. Aringhieri, Nanoporosity characteristics of some natural clay minerals and soils, Clays Clay Minerals 52 (6) (2004) 700–704.
[18] C.-C. Wang, et al., Effects of exchanged surfactant cations on the pore structure and adsorption characteristics of montmorillonite, J. Colloid Interface Sci. 280 (1) (2004) 27–35.
[19] C.D. Jenkins, Coalbed- and shale-gas reservoirs, J. Petroleum Technol. 60 (2) (2008) 92–99.
[20] D.J.K. Ross, R. Marc Bustin, The importance of shale composition and pore structure upon gas storage potential of shale gas reservoirs, Mar. Petroleum Geol. 26 (6) (2009) 916–927.
[21] M. Gasparik, et al., The methane storage capacity of black shales, in: 3rd EAGE Shale Wrokshop, 2012.
[22] Z. Jin, A. Firoozabadi, Effect of water on methane and carbon dioxide sorption in clay minerals by Monte Carlo simulations, Fluid Phase Equilibria 382 (2014) 10–20.
[23] A. Busch, Y. Gensterblum, B.M. Krooss, Methane and CO2 sorption and desorption measurements on dry Argonne premium coals: pure components and mixtures, Int. J. Coal Geol. 55 (2–4) (2003) 205–224.
[24] A. Hildenbrand, et al., Evolution of methane sorption capacity of coal seams as a function of burial history — a case study from the Campine Basin, NE Belgium, Int. J. Coal Geol. 66 (3) (2006) 179–203.
[25] R. Lahann, et al., Influence of CO2 on New Albany Shale composition and pore structure, Int. J. Coal Geol. 108 (0) (2013) 2–9.
[26] S.M. Kang, et al., Carbon dioxide storage capacity of organic-rich shales, SPE J. 16 (4) (2011) 842–855.
[27] A.K. Dahaghi, Numerical simulation and modeling of enhanced gas recovery and CO2 sequestration in shale gas reservoirs: a feasibility study, in: SPE International Conference on CO2 Capture, Storage, and Utilization, Society of Petroleum Engineers, New Orleans, Louisiana, 2010.
[28] Q. Yuan, et al., Molecular dynamics simulations of the enhanced recovery of confined methane with carbon dioxide, Phys. Chem. Chem. Phys. 17 (47) (2015) 31887–31893.
[29] H. Wu, J. Chen, H. Liu, Molecular dynamics simulations about adsorption and displacement of methane in carbon nanochannels, J. Phys. Chem. C 119 (24) (2015) 13652–13657.
[30] P. Kowalczyk, et al., Displacement of methane by coadsorbed carbon dioxide is facilitated in narrow carbon nanopores, J. Phys. Chem. C 116 (25) (2012) 13640–13649.
[31] M. Firouzi, J. Wilcox, Slippage and viscosity predictions in carbon micropores and their influence on CO2 and CH4 transport, J. Chem. Phys. 138 (6) (2013) 064705.
[32] S.P. Neuman, Theoretical derivation of Darcy's law, Acta Mech. 25 (3–4) (1977) 153–170.
[33] S. Whitaker, Flow in porous media I: a theoretical derivation of Darcy's law, Transp. Porous Media 1 (1) (1986) 3–25.
[34] K.P. Travis, B.D. Todd, D.J. Evans, Departure from Navier-Stokes hydrodynamics in confined liquids, Phys. Rev. E 55 (4) (1997) 4288–4295.
[35] Z. Jin, A. Firoozabadi, Flow of methane in shale nanopores at low and high pressure by molecular dynamics simulations, J. Chem. Phys. 143 (104315)

(2015).
[36] J.K. Holt, et al., Fast mass transport through sub-2-nanometer carbon nanotubes, Science 312 (5776) (2006) 1034–1037.
[37] L.J. Klinkenberg, The Permeability of Porous Media to Liquids and Gases, in Drilling and Production Practice, American Petroleum Institute, 1941.
[38] Y.-S. Wu, K. Pruess, P. Persoff, Gas flow in porous media with Klinkenberg effects, Transp. Porous Media 32 (1) (1998) 117–137.
[39] F. Javadpour, Nanopores and apparent permeability of gas flow in mudrocks (shales and siltstone), J. Can. Petroleum Technol. 48 (8) (2009) 16–21.
[40] C. Cottin-Bizonne, et al., Low-friction flows of liquid at nanopatterned interfaces, Nat. Mater 2 (4) (2003) 237–240.
[41] S.K. Bhatia, O. Jepps, D. Nicholson, Tractable molecular theory of transport of Lennard-Jones fluids in nanopores, J. Chem. Phys. 120 (9) (2004) 4472–4485.
[42] S.K. Bhatia, D. Nicholson, Transport of simple fluids in nanopores: theory and simulation, AIChE J. 52 (1) (2006) 29–38.
[43] R. Krishna, J.M. van Baten, Unified Maxwell–Stefan description of binary mixture diffusion in micro- and meso-porous materials, Chem. Eng. Sci. 64 (13) (2009) 3159–3178.
[44] R. Krishna, J.M. van Baten, An investigation of the characteristics of Maxwell–Stefan diffusivities of binary mixtures in silica nanopores, Chem. Eng. Sci. 64 (5) (2009) 870–882.
[45] J. Collell, et al., Transport of multicomponent hydrocarbon mixtures in shale organic matter by molecular simulations, J. Phys. Chem. C 119 (39) (2015) 22587–22595.
[46] S. Wang, F. Javadpour, Q. Feng, Molecular dynamics simulations of oil transport through inorganic nanopores in shale, Fuel 171 (2016) 74–86.
[47] S. Wang, F. Javadpour, Q. Feng, Fast mass transport of oil and supercritical carbon dioxide through organic nanopores in shale, Fuel 181 (2016) 741–758.
[48] M. Kazemi, A. Takbiri-Borujeni, Non-equilibrium molecular dynamics simulation of gas flow in organic nanochannels, J. Nat. Gas Sci. Eng. 33 (2016) 1087–1094.
[49] B. Widom, Some topics in the theory of fluids, J. Chem. Phys. 39 (11) (1963) 2808–2812.
[50] M.G. Martin, J.I. Siepmann, Transferable potentials for phase equilibria. 1. United-atom description of n-alkanes, J. Phys. Chem. B 102 (14) (1998) 2569–2577.
[51] P. van der Ploeg, H.J.C. Berendsen, Molecular dynamics simulation of a bilayer membrane, J. Chem. Phys. 76 (6) (1982) 3271–3276.
[52] W.L. Jorgensen, J.D. Madura, C.J. Swenson, Optimized intermolecular potential functions for liquid hydrocarbons, J. Am. Chem. Soc. 106 (22) (1984) 6638–6646.
[53] H.J.C. Berendsen, J.R. Grigera, T.P. Straatsma, The missing term in effective pair potentials, J. Phys. Chem. 91 (24) (1987) 6269–6271.
[54] J.G. Harris, K.H. Yung, Carbon Dioxide's liquid-vapor coexistence curve and critical Properties as Predicted by a simple molecular model, J. Phys. Chem. 99 (31) (1995) 12021–12024.
[55] I.-C. Yeh, M.L. Berkowitz, Ewald summation for systems with slab geometry, J. Chem. Phys. 111 (7) (1999) 3155–3162.
[56] P.S. Crozier, et al., Comparison of charged sheets and corrected 3D Ewald calculations of long-range forces in slab geometry electrolyte systems with solvent molecules, J. Chem. Phys. 112 (21) (2000) 9253–9257.
[57] W.A. Steele, The physical interaction of gases with crystalline solids: I. Gas-solid energies and properties of isolated adsorbed atoms, Surf. Sci. 36 (1) (1973) 317–352.
[58] S. Wang, Y. Yu, G. Gao, Non-equilibrium molecular dynamics simulation on pure gas permeability through carbon membranes, Chin. J. Chem. Eng. 14 (2) (2006) 164–170.
[59] S.-M. Wang, Y.-X. Yu, G.-H. Gao, Grand canonical Monte Carlo and non-equilibrium molecular dynamics simulation study on the selective adsorption and fluxes of oxygen/nitrogen gas mixtures through carbon membranes, J. Membr. Sci. 271 (1–2) (2006) 140–150.
[60] W.C. Swope, et al., A computer simulation method for the calculation of equilibrium constants for the formation of physical clusters of molecules: Application to small water clusters, J. Chem. Phys. 76 (1) (1982) 637–649.
[61] H.J.C. Berendsen, et al., Molecular dynamics with coupling to an external bath, J. Chem. Phys. 81 (8) (1984) 3684–3690.
[62] M.P. Allen, D.J. Tildesley, Computer Simulation of Liquids, Clarendon, , Oxford, 1987.
[63] G.S. Heffelfinger, F.v. Swol, Diffusion in Lennard-Jones fluids using dual control volume grand canonical molecular dynamics simulation (DCV-GCMD), J. Chem. Phys. 100 (10) (1994) 7548–7552.
[64] D.M. Ford, G.S. Heffelfinger, Massively parallel dual control volume grand canonical molecular dynamics with LADERA II. Gradient driven diffusion through polymers, Mol. Phys. 94 (4) (1998) 673–683.
[65] L. Xu, et al., Nonequilibrium molecular dynamics simulation of transport of gas mixtures in nanopores, Phys. Rev. Lett. 80 (16) (1998) 3511.
[66] A. Papadopoulou, et al., Molecular dynamics and Monte Carlo simulations in the grand canonical ensemble: local versus global control, J. Chem. Phys. 98 (6) (1993) 4897–4908.
[67] A. Vieira-Linhares, N. Seaton, Non-equilibrium molecular dynamics simulation of gas separation in a microporous carbon membrane, Chem. Eng. Sci. 58 (18) (2003) 4129–4136.
[68] L. Lu, Q. Wang, Y. Liu, Adsorption and separation of ternary and quaternary mixtures of short linear alkanes in zeolites by molecular simulation, Langmuir 19 (25) (2003) 10617–10623.
[69] W.-Z. Li, et al., Molecular simulation of adsorption and separation of mixtures of short linear alkanes in pillared layered materials at ambient temperature, J. Colloid Interface Sci. 312 (2) (2007) 179–185.